Materials Research Bulletin 63 (2015) 6–12

Contents lists available at ScienceDirect

Materials Research Bulletin

journal homepage: www.elsevier.com/locate/matresbu

Structural, magnetic, and electrochemical properties of $LiMn_{1-x}Ni_xPO_4$

A. Ottmann [a,*], C. Jähne [a], H.-P. Meyer [b], R. Klingeler [a,c]

[a] Kirchhoff Institute for Physics, Heidelberg University, 69120 Heidelberg, Germany
[b] Institute of Earth Sciences, Heidelberg University, 69120 Heidelberg, Germany
[c] Centre for Advanced Materials, Heidelberg University, 69120 Heidelberg, Germany

ARTICLE INFO

Article history:
Received 23 June 2014
Received in revised form 31 October 2014
Accepted 2 November 2014
Available online 6 November 2014

Keywords:
B. Solvothermal
C. X-ray diffraction
D. Electrochemical properties
D. Magnetic properties

ABSTRACT

A solid solutions series of $LiMn_{1-x}Ni_xPO_4$ nanomaterials with $0 \leq x \leq 0.45$ was produced by a low-temperature microwave-assisted hydrothermal process. The materials have been systematically studied regarding structure, morphology, magnetism, and electrochemical properties. The lattice parameters in the orthorhombic olivine structure obey Vegard's law and linearly depend on x. Similarly, the static magnetisation reflects the decrease of the transition metal paramagnetic moment upon substitution of Mn^{2+} by Ni^{2+}. At low temperatures, antiferromagnetic long range order appears for all Ni-concentrations. The potential of the $Mn^{2+/3+}$ redox couple is found to linearly increase with x. This is explained by a larger electronegativity of Ni^{2+} as compared to Mn^{2+} and associated changes in the covalency of the Mn–O bond.

1. Introduction

Since the introduction of $LiFePO_4$ as cathode material for lithium-ion batteries by Padhi et al. in 1997 [1], plenty of research has been dedicated to the olivine-structured orthophosphates. Major efforts focus on enhancing the poor electronic conductivity and ionic diffusivity in these materials [2,3], which is essential for application in lithium-ion batteries. In the case of $LiFePO_4$, these efforts resulted in a low cost, environmentally benign, and thermally stable material, which is applied commercially [4,5]. Due to the demand for higher energy densities, the phospho-olivines $LiMPO_4$ with M = Mn, Co, Ni are gaining increasing attention, as the redox couples exhibit a considerably higher potential vs. lithium, namely 4.1 V ($Mn^{2+/3+}$), 4.8 V ($Co^{2+/3+}$) and 5.2 V ($Ni^{2+/3+}$) [6–8]. $LiMnPO_4$ is of particular interest because the operating voltage does not exceed the electrochemical stability window of conventional electrolytes [9] and manganese is abundant as well as nontoxic. However, $LiMnPO_4$ features poor electrochemical properties due to an even lower electronic conductivity compared to $LiFePO_4$ and a Jahn–Teller distortion associated with Mn^{3+} in the delithiated phase [10–12]. Nanoscaling and Mn-site doping are promising approaches to overcome these drawbacks [13]. To be specific, Mn-site doping with smaller ions, e.g. Ni^{2+}, has been found to attenuate the lattice distortion, thereby improving the electrochemical performance [14,15]. Furthermore, mixed transition metal ion orthophosphates $LiM_{1-x}M'_xPO_4$ (M, M′ = Fe, Mn, Co) show an increase of the cell voltage [16], which presents an additional way to boost the energy density of cathode materials.

While conventional hydrothermal methods have been well established for decades, the more recent microwave-assisted approach combines the low-temperature synthesis with particularly short reaction times [17]. Moreover, it allows to tailor the size, morphology, and chemical composition of the product materials [18,19]. In case of the phospho-olivines, the hydrothermal route has been successfully applied to synthesise a broad range of doped and mixed transition metal compounds [17,20–23]. In the present work, a modified glycol-based synthesis protocol from Ref. [22] was adapted to obtain a $LiMn_{1-x}Ni_xPO_4$ doping series in 5%-steps up to $x = 0.45$. The data show solid solution behaviour with decreasing unit cell volume towards $LiMn_{0.55}Ni_{0.45}PO_4$, corresponding to Vegard's law and a rising reduction potential of the $Mn^{2+/3+}$ couple.

2. Experimental

$LiMn_{1-x}Ni_xPO_4$ powder samples were synthesised via a microwave-assisted hydrothermal route (cf. Ref. [24]). At first, manganese(II) and nickel(II) acetate tetrahydrate (Sigma–Aldrich) were dissolved in ethylene glycol (EG, Sigma–Aldrich) in a molar ratio of $(1-x):x$ with a total concentration of 0.03 mol l^{-1}. 10 ml of this solution was poured in a 30 ml glass vessel and aqueous solutions of lithium hydroxide (Sigma–Aldrich) and phosphoric

* Corresponding author. Tel.: +49 6221549819; fax: +49 6221549869.
E-mail address: alex.ottmann@kip.uni-heidelberg.de (A. Ottmann).

http://dx.doi.org/10.1016/j.materresbull.2014.11.008
0025-5408/

acid (85%, Merck) with concentrations of 1.5 mol l^{-1} and 1.0 mol l^{-1}, respectively, were added to obtain a (Mn+Ni):Li:P molar ratio of 1:1:1. The resulting mixture was heated in a *Monowave 300* (Anton Paar) microwave reactor within 10 min to 300 °C and kept at this temperature for 15 min while being stirred at 300 rpm. Natural cooling to room temperature was supported by compressed air flow inside the reactor. The resulting precipitate was recovered and washed five times by adding 12 ml of ethanol, centrifugating the suspension at 5000 rpm for 5 min and removing supernatant solution to ensure that no ethylene glycol and soluble precursors were left. Yields from three consecutive syntheses with the same precursor solution were dispersed together in ethanol in order to obtain the final product. Finally, this mixture was dried at ca. 100 °C overnight.

X-ray powder diffraction (XRD) was carried out on a Siemens *D500* in Bragg-Brentano geometry, applying Cu-$K_{\alpha 1}$ radiation and 2θ angle steps of 0.01°. Rietveld refinement with a pseudo-Voigt-type profile was done with the FullProf program [25]. This analysis was based on structure parameters for $LiMnPO_4$ (ICSD #99858 [26]). The morphology was studied by means of scanning electron microscopy (SEM) on a Zeiss *LEO 1530*. Elemental analyses were done by means of energy-dispersive X-ray spectrometry (EDX) on a *LEO 440*. Preliminarily, the samples were coated with gold (morphology studies) or carbon (elemental analyses), respectively. The calibration of the EDX-detector was checked by measuring the well-known end member $LiMnPO_4$. Magnetic properties have been determined with a Quantum Design *MPMS-2* after cooling in zero magnetic field (zfc).

Electrochemical characterisation by means of cyclic voltammetry was performed in two-electrode Swagelok-type cells vs. lithium metal with a *VMP3* multichannel potentiostat (Bio-Logic). The working electrodes were prepared from a mixture of pristine $LiMn_{1-x}Ni_xPO_4$ powders with carbon black (Timcal) and polyvinylidene fluoride (PVDF) binder (Solvay Plastics) in a weight ratio of 75:20:5. This mixture was pestled in a mortar under dropwise addition of N-methyl-2-pyrrolidone (NMP, Sigma–Aldrich). Around 4 mg of the resulting slurry was pasted on alumina meshes with a diameter of 10 mm, dried in vacuum at 100 °C overnight, pressed with 10 MPa and dried at 100 °C again. The cells were assembled in an Ar-atmosphere glove box (O_2/H_2O <1 ppm), where the working electrode and a lithium metal foil disk (Alfa Aesar), which had been pressed on a nickel current collector, were merged. Both electrodes were separated by two layers of glass microfibre (Whatman *GF/D*), soaked with 200 µl electrolyte. A 1 molar solution of $LiPF_6$ in 1:1 ethylene carbonate (EC)/dimethyl carbonate (DMC) was used as an electrolyte (Merck Electrolyte *LP30*). The active material mass per mesh area averaged 3.8 mg cm^{-2}. Electrochemical cycling was performed in the potential range 3.5–4.5 V at a scan rate of 0.05 mV s^{-1}, and in a climate chamber that was at 25 °C.

3. Results and discussion

The synthesis yields polycrystalline powders whose colour and morphology depend on the ratio between manganese and nickel in the precursor solution. Upon increasing the Ni content, the colour changes from cream white to light orange. Concomitantly, needle-like structures observed for $x = 0$ change to rhomb-like platelets, as displayed in the SEM images shown in Fig. 1. Since all synthesis parameters except the Mn:Ni ratio are kept constant, one has to conclude that differences between the transition metal ions are governing the morphology changes. Following Refs. [27,19] suggest that differences in acidity and electronegativity are key factors. To be specific, Mn^{2+} (Ni^{2+}) shows $pK_a = 10.59$ (9.86) and EN = 1.55 (1.91) [28]. One may hence speculate that in case of Ni^{2+}, the crystallite surfaces are decorated more efficiently by OH^- and EG–O^- which affects the crystal growth accordingly.

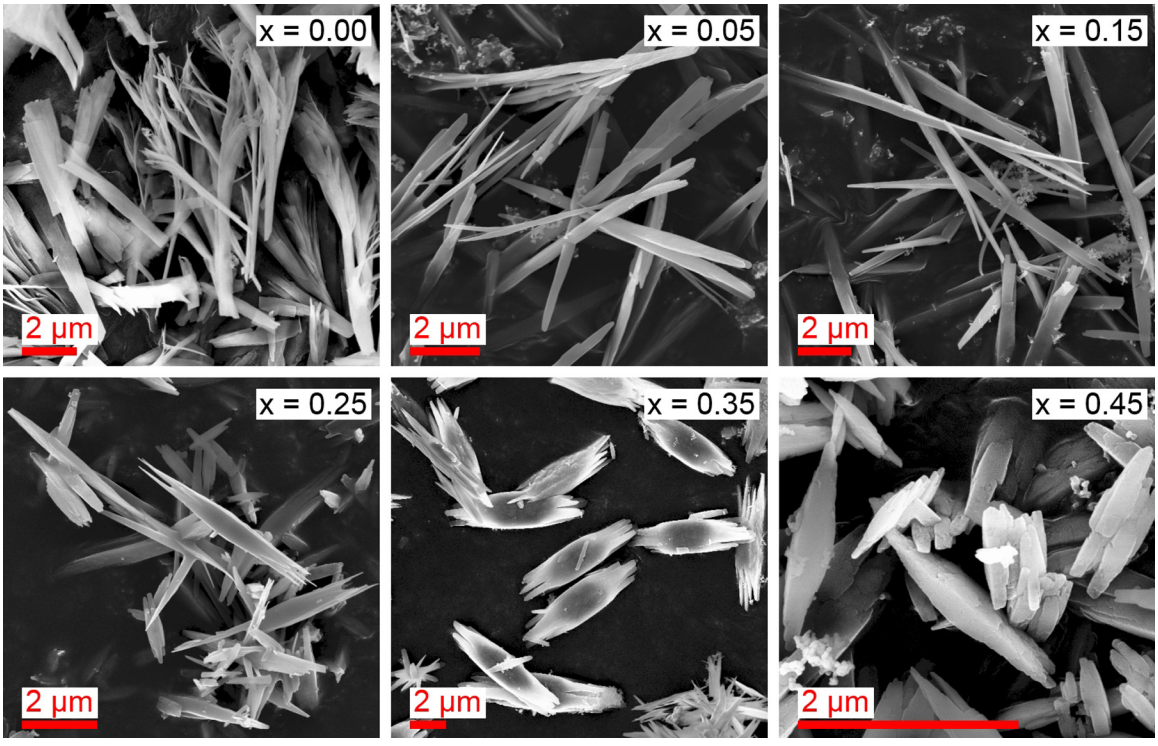

Fig. 1. SEM images of pristine $LiMn_{1-x}Ni_xPO_4$ with $0 \leq x \leq 0.45$.

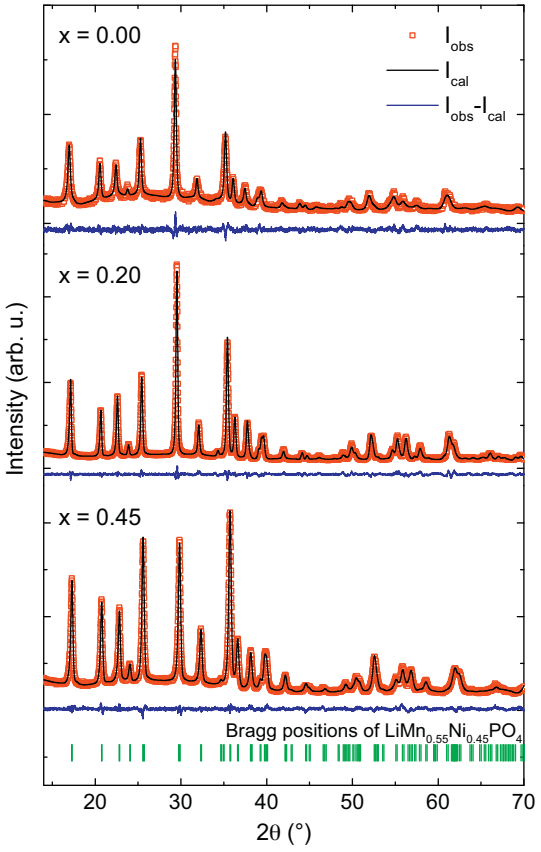

Fig. 2. XRD powder patterns of $LiMn_{1-x}Ni_xPO_4$ with $x = 0$, 0.2, and 0.45 obtained at $2\Theta = 14–70^\circ$ and Rietveld refinement based on ICSD #99858 [26]. Symbols represent the observed intensity I_{obs} and the red line the calculated intensity I_{calc}. (For interpretation of the references to colour in this figure legend, the reader is referred to the web version of the article.)

3.1. Structure and composition

Fig. 2 shows XRD patterns of $LiMn_{1-x}Ni_xPO_4$ with nominal Ni-contents $x = 0$, 0.2, and 0.45. The nominal Ni-content is taken from the Ni:Mn-ratio in the precursor solution. All Bragg peaks of the three samples can be indexed based on an olivine-like $LiMnPO_4$ structure with *Pnma* space group (ICSD #99858 [26]). The absence of additional diffraction peaks indicates phase pure materials.[1] We note that our synthesis procedure yields significant impurity phases for precursor solutions with nominal Ni-contents $x \geq 0.5$. Rietveld refinement based on ICSD #99858, using an additional position for the nickel ion, is found in good agreement with the measured intensities, as evident if the residua ($I_{obs} - I_{calc}$) and the low χ^2 values are considered (Fig. 2). To achieve such a good agreement, the atomic positions for manganese and nickel were refined independently from each other, what lead to a deviation between those positions.

The effect of Ni-doping is qualitatively seen in Fig. 3, which displays the XRD pattern in the range $2\theta = 29–30^\circ$ for five different x exemplarily. The data highlight a shift of the overlapping (2 1 1)/(0 2 0) diffraction peaks to larger angles with increasing nickel concentration. This behaviour indicates a clear change of the lattice parameters. For a quantitative analysis, structure refinement was done for all nominal Ni-concentrations $0 \leq x \leq 0.45$ in order to obtain the lattice parameters. The results of the analysis and the

[1] Only for $x = 0.3$ and 0.4, the XRD data show minor impurity peaks, which can be attributed to Li_3PO_4.

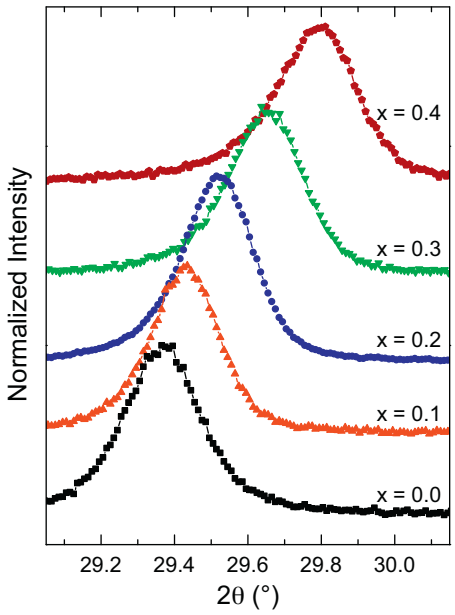

Fig. 3. Shift of the merged (2 1 1)/(0 2 0) XRD diffraction peak for different Ni-concentrations.

resulting cell volume are displayed in Fig. 4. The unit cell volume for $x = 0$ agrees well with the single crystal data from Ref. [29]. The data imply a linear decrease of all lattice parameters upon increasing the nominal Ni-content. Quantitatively, the unit cell volume shrinks from 300.6 ± 0.4 Å^3 in $LiMnPO_4$ to 288.0 ± 0.4 Å^3 in $LiMn_{0.55}Ni_{0.45}PO_4$, i.e. there is a relative change of $\Delta V/V = -9e{-}4/\%$ Ni. The result agrees very well with recent single crystal data for $LiMn_{0.95}Ni_{0.05}PO_4$ which suggest $\Delta V/V \approx -1e{-}3/\%$ Ni [30]. The reduced unit cell volume may be attributed to negative chemical pressure due to the different ionic radii of Mn^{2+} (0.83 Å) and Ni^{2+} (0.69 Å) [31].

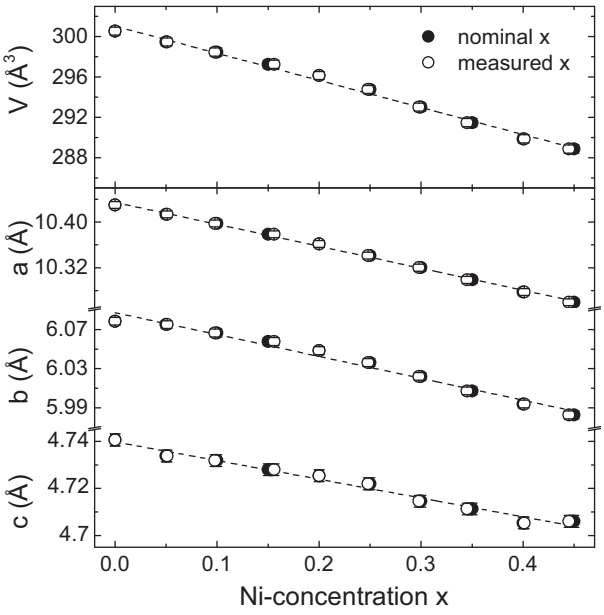

Fig. 4. Lattice parameters *a*, *b*, and *c* (space group *Pnma*) and resulting unit cell volume *V* of $LiMn_{1-x}Ni_xPO_4$ vs. Ni-content *x*. Filled symbols refer to nominal *x*, open ones to refined values.

Table 1
Nominal Ni-content x in $LiMn_{1-x}Ni_xPO_4$ and refined one as determined by analysis of the EDX spectra (see the text).

nominal x ($\% \pm 0.1\,\%$)	0.0	5.1	10.0	15.0	20.0	25.0	30.0	35.0	40.0	45.0
refined x ($\% \pm 0.5\,\%$)	0.0	5.1	9.8	15.6	20.0	24.8	29.8	34.5	40.1	44.5

Chemical analyses were performed by means of energy-dispersive X-ray spectrometry in order to obtain the actual Ni-content in the materials. For each material, five different spots with 1.2 μm diameter have been measured for deriving the chemical composition. The Li-content generally cannot be obtained by EDX measurement. Oxygen was not determined from the spectra either, but assumed to be stoichiometric with the cations Mn^{2+}, Ni^{2+}, and P^{5+}. Accordingly, when normalising to 100%, Li_2O was neglected. The atomic ratios of Ni to Mn + Ni, obtained from the analyses of the EDX spectra, are shown in Table 1 where they are compared with the nominal ones from the precursor solution. The statistical uncertainty as determined by the root mean square deviations from the average values amounts to about 0.5%.

The average Mn:Ni ratio as determined from the EDX data agrees well with the nominal one which indicates that all the initially used nickel is incorporated in the olivine-structured main phase of $LiMn_{1-x}Ni_xPO_4$ and has a rather homogenous Ni-distribution. This result agrees with the fact that the concentration dependence of the lattice parameters follows Vegard's law. Thus, the XRD data corroborate that a series of solid solutions of $LiMn_{1-x}Ni_xPO_4$ with $0 \le x \le 0.45$ is formed. Concomitantly, the coexistence of phases with deviating x is excluded.

3.2. Magnetic properties

Fig. 5 presents the temperature dependence of the molar static magnetic susceptibility $\chi_m = M/B$ of $LiMnPO_4$ and its inverse in an external magnetic field of $B = 0.5$ T. At high temperatures, the data obey a Curie–Weiss-like behaviour $\chi = \chi_0 + (N_A\mu_{eff}^2)/(3k_B(T-\theta))$, with χ_0 being a temperature independent contribution, N_A the Avogadro number, μ_{eff} the effective magnetic moment, k_B the Boltzmann constant, and θ the Weiss temperature. Fitting the data by means of the Curie–Weiss law yields $\mu_{eff} = 5.90(5)\,\mu_B$, $\theta = -68(3)$ K, and $\chi_0 \approx 0$. The obtained effective moment agrees with the expected spin-only value of Mn^{2+} for $S = 5/2$, supposing a g-factor of 1.98 [29]. The negative Weiss temperature implies antiferromagnetic interactions. Indeed, long range antiferromagnetic order is found below $T_N = 32$ K. The Néel temperature has been determined by calculating the magnetic specific heat which is proportional to $\partial(\chi_m T)/\partial T$. It shows a λ-like anomaly, whose maximum signals T_N (see inset Fig. 5).

At doping levels $x \ge 0.05$ the data do not allow a reliable Curie–Weiss analysis. However, the molar magnetisation M at 300 K and the Néel temperature T_N allow assessing the influence of nickel doping on the magnetic properties. Like in $LiMnPO_4$, the Néel temperature of every sample has been deduced from the maximum of the magnetic specific heat, which is depicted in Fig. 6. Fig. 7(a) shows that the room temperature magnetisation of $LiMn_{1-x}Ni_xPO_4$ linearly decreases with increasing x. This change can be attributed to the overall effective magnetic moment which is supposed to decrease upon Ni doping due to the smaller magnetic moment of Ni^{2+} compared to Mn^{2+}. To be more specific, the spin-only magnetic moment of Ni^{2+} amounts to 2.83 μ_B in an octahedral crystal field, which is much smaller than $\mu_{eff} = 5.90(5)\,\mu_B$ found for Mn^{2+}.

In contrast to the linear x-dependence of M(300 K), there is no consistent trend in $T_N(x)$ (Fig. 7(b)). One may separate two regions, one of which covers $0 \le x \le 0.15$ where T_N decreases significantly and linearly in x. At higher doping levels, the doping dependence is

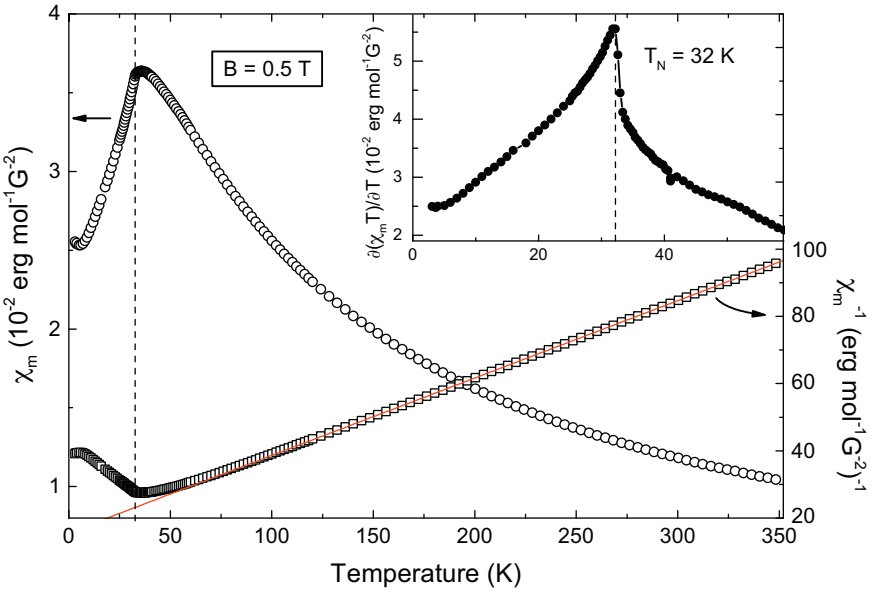

Fig. 5. Molar static magnetic susceptibility χ_m of $LiMnPO_4$ and its inverse χ_m^{-1} vs. temperature. The red line displays a Curie–Weiss fit to the high-temperature data (≥148 K). Inset: Magnetic specific heat $\partial(\chi_m T)/\partial T$, which is used to determine T_N (dashed line). (For interpretation of the references to colour in this figure legend, the reader is referred to the web version of the article.)

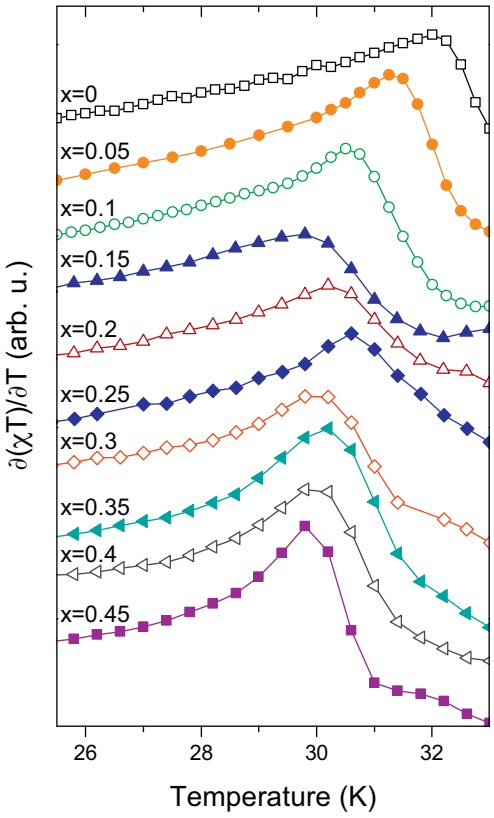

Fig. 6. Magnetic specific heat of $LiMn_{1-x}Ni_xPO_4$, the maximum position of which signals T_N.

much less pronounced. Note that the end member $LiNiPO_4$ exhibits T_N = 25 K [32]. However, there are different magnetic ground states in $LiMnPO_4$ and $LiNiPO_4$, including different magnetic easy axes [32,33]. The behaviour in the low-doping range $0 \leq x \leq 0.15$ may be related to the fact that the easy axis anisotropy decreases upon Ni-doping. For $x = 0$, the spin-flop transition at $T = 2$K amounts to $B_{SF} = 4$ T which decreases to $B_{SF} = 2.8$ T at $x = 0.05$ [30,34]. One may hence speculate that the non-linear doping dependence of T_N present in our data may be associated with vanishing uniaxial anisotropy and/or change of the magnetic ground state at a Ni-concentration around $x \approx 0.2$.

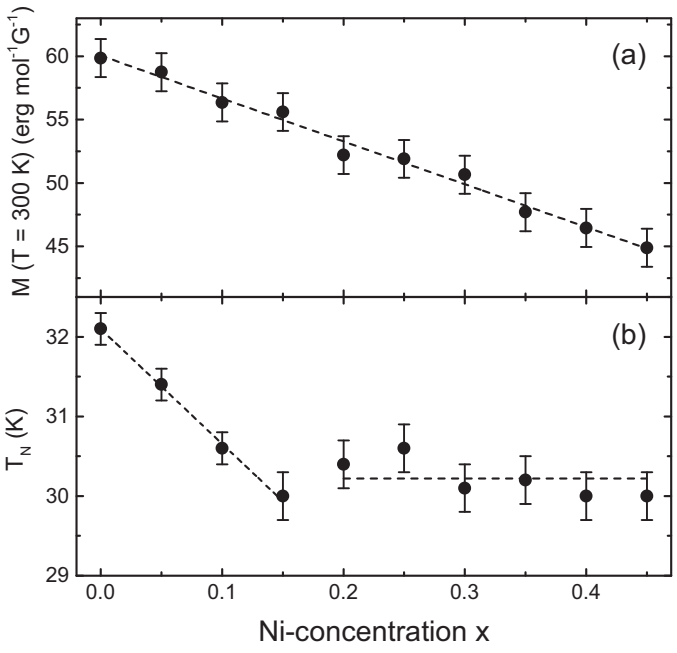

Fig. 7. (a) Magnetisation of $LiMn_{1-x}Ni_xPO_4$ at 300 K and (b) Néel temperature T_N vs. nominal Ni-concentration x. Lines are guides to the eye.

3.3. Cyclic voltammetry

Cyclic voltammetry was applied for the electrochemical characterisation of the materials. Fig. 8(a) shows the 1st, 2nd, 5th and 10th cycle of a cyclic voltammogram (CV) for $LiMnPO_4$, starting at the open cell voltage of 3.2 V vs. $Li^{0/+}$. Both an oxidation peak at around 4.35 V and a reduction peak at 3.96–3.97 V are visible in all recorded cycles. They can be attributed to the $Mn^{2+/3+}$ redox couple in $LiMnPO_4$ [35]. Above 4.4 V, an additional contribution to the current is detected, which is attributed to the onset of electrolyte decomposition and the reaction of the decomposition products with the active material [36,37]. The observed decrease of the oxidative current density with increasing number of cycles can possibly be attributed to the formation of a surface layer similar to the solid electrolyte interface (SEI) on carbon electrodes [38]. This may protect the active material against further reaction with the decomposition products of the

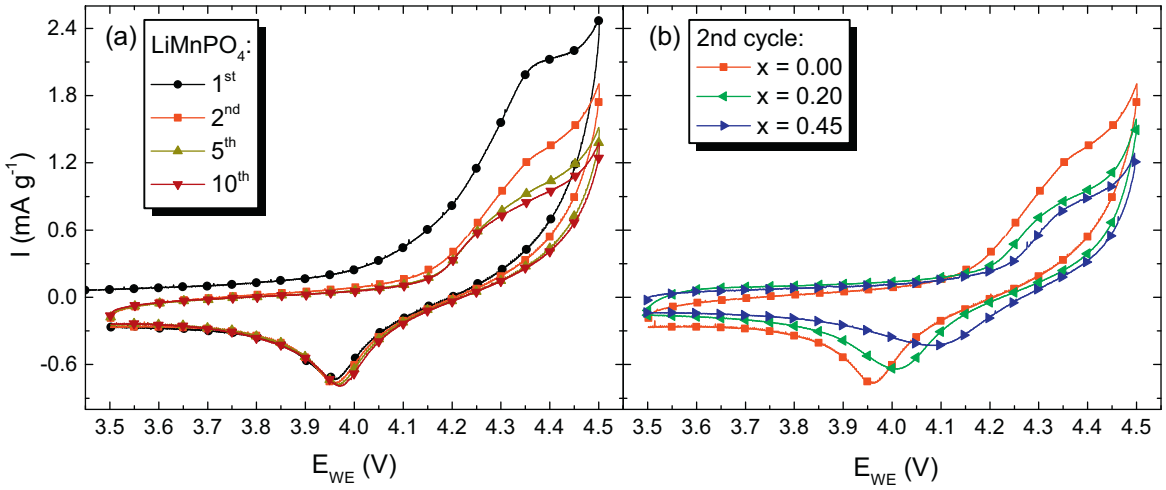

Fig. 8. (a) Cyclic voltammograms of $LiMnPO_4$ and (b) a comparison of the 2nd cycle for $LiMnPO_4$, $LiMn_{0.8}Ni_{0.2}PO_4$ and $LiMn_{0.55}Ni_{0.45}PO_4$, measured at a scan rate of 0.05 mV s^{-1}.

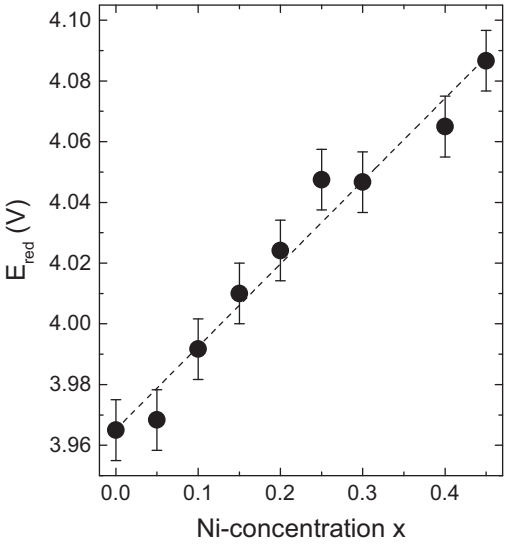

Fig. 9. Averaged reduction peak potentials vs. $Li^{0/+}$ of $LiMn_{1-x}Ni_xPO_4$.

electrolyte. Note that the peak positions and the reduction peak current density barely change upon cycling, which indicates a good reversibility of the $Mn^{2+/3+}$ redox reaction.

A comparison of the second CV cycles of $LiMn_{1-x}Ni_xPO_4$ with $x = 0$, 0.2, and 0.45, shown in Fig. 8(b), provides information about the effect of changing the Ni-concentration on the abovementioned redox couple. Note that the redox couple $Ni^{2+/3+}$ is not accessible with the applied experimental setup because its expected active potential range above 5 V [8] exceeds the electrolyte's stability window [9]. The data display two clear trends, which are likewise supported by the CVs of all samples (not shown). Firstly, the peak current densities decrease with increasing x. This effect may be straightforwardly attributed to the fact that the Mn-content in the materials is decreasing upon increasing x, since the $Mn^{2+/3+}$ redox couple is the electrochemically active element in the potential range under study. Secondly, the data show that the position of the reduction peak continuously shifts to higher voltages with increasing x.

Fig. 9 illustrates this observation for the different doping levels by presenting the averaged potential E_{red} (as derived from the 2nd, 5th and 10th cycle) of the reduction peak as a function of the Ni-content in $LiMn_{1-x}Ni_xPO_4$. The data imply a linear increase of E_{red} with x. Throughout the whole doping series, E_{red} increases by 3% from 3.97 V in $LiMnPO_4$ to 4.09 V in $LiMn_{0.55}Ni_{0.45}PO_4$. Similar effects of linear x-dependence of the redox potential have been observed, e.g. in $LiFe_{1-x}Co_xPO_4$ and $LiMn_{1-x}Co_xPO_4$ solid solutions [16]. Following the arguments given in Ref. [16], changes in the electronegativity (EN) of the transition metal ions is the crucial parameter governing this behaviour. In the case of $LiMn_{1-x}Ni_xPO_4$ studied here, the partial substitution of Mn^{2+} with EN 1.55 [28] by the more electronegative Ni^{2+} (EN 1.91 [28]) reduces the covalency of the Mn–O bond which leads to the experimentally observed increase of the $Mn^{2+/3+}$ redox potential.

4. Conclusions

A solid solutions series of $LiMn_{1-x}Ni_xPO_4$ nanomaterials with $0 \leq x \leq 0.45$ was produced by a low-temperature microwave-assisted hydrothermal process. The materials have been systematically studied by means of X-ray diffraction, scanning electron microscopy (including EDX), magnetic studies, and cyclic voltammetry. The materials feature an orthorhombic olivine-like structure and obey Vegard's law. To be specific, the lattice parameters and the unit cell volumes linearly depend on x. The static magnetic properties reflect the decrease of the transition metal paramagnetic moment upon substitution of Mn^{2+} by Ni^{2+}. In addition, the data imply an antiferromagnetic ground state for all Ni-concentrations. While there are only small effects of Ni-substitution on the Néel ordering temperature, the non-linear T_N (x) dependence possibly indicates a change of the magnetic ground state around $x \approx 0.2$. Electrochemically, the potential of the $Mn^{2+/3+}$ redox couple is found to linearly increase with x, which is explained by a larger electronegativity of Ni^{2+} as compared to Mn^{2+} and associated changes in the covalency of the Mn–O bond.

Acknowledgements

The authors thank I. Glass for experimental support. Financial support by the Bundesministerium für Bildung und Forschung (03SF0397) and by Deutsche Forschungsgemeinschaft (KL 1824/2-2) are gratefully acknowledged.

References

[1] A.K. Padhi, K.S. Nanjundaswamy, J.B. Goodenough, Phospho-olivines as positive-electrode materials for rechargeable lithium batteries, J. Electrochem. Soc. 144 (4) (1997) 1188.
[2] B.L. Ellis, K.T. Lee, L.F. Nazar, Positive electrode materials for Li-ion and Li-batteries, Chem. Mater. 22 (3) (2010) 691.
[3] K. Zaghib, A. Mauger, C.M. Julien, Overview of olivines in lithium batteries for green transportation and energy storage, J. Solid State Electrochem. 16 (3) (2012) 835.
[4] M. Takahashi, S. Tobishima, K. Takei, Y. Sakurai, Reaction behavior of $LiFePO_4$ as a cathode material for rechargeable lithium batteries, Solid State Ionics 148 (3-4) (2002) 283.
[5] L.-X. Yuan, Z.-H. Wang, W.-X. Zhang, X.-L. Hu, J.-T. Chen, Y.-H. Huang, J.B. Goodenough, Development and challenges of $LiFePO_4$ cathode materials for lithium-ion batteries, Energy Environ. Sci. 4 (2) (2011) 269.
[6] G. Li, H. Azuma, M. Tohda, $LiMnPO_4$ as the cathode for lithium batteries, Electrochem. Solid State Lett. 5 (6) (2002) A135.
[7] K. Amine, H. Yasuda, M. Yamachi, Olivine $LiCoPO_4$ as 4.8 V electrode material for lithium batteries, Electrochem. Solid-State Lett. 3 (4) (2000) 178.
[8] J. Wolfenstine, J. Allen, Ni^{3+}/Ni^{2+} redox potential in $LiNiPO_4$, J. Power Sources 142 (2005) 389.
[9] K. Xu, Nonaqueous liquid electrolytes for lithium-based rechargeable batteries, Chemical Reviews 104 (10) (2004) 4303.
[10] C. Delacourt, L. Laffont, R. Bouchet, C. Wurm, J.-B. Leriche, M. Morcrette, J.-M. Tarascon, C. Masquelier, Toward understanding of electrical limitations (electronic, ionic) in $LiMPO_4$ (M = Fe, Mn) electrode materials, J. Electrochem. Soc. 152 (5) (2005) 913.
[11] A. Yamada, M. Hosoya, S.-C. Chung, Y. Kudo, K. Hinokuma, K.-Y. Liu, Y. Nishi, Olivine-type cathodes, J. Power Sources 119–121 (2003) 232.
[12] C. Rudisch, H.-J. Grafe, J. Geck, S. Partzsch, M.V. Zimmermann, N. Wizent, R. Klingeler, B. Buechner, Coupling of Li-motion and structural distortions in olivine $LiMnPO_4$ from 7Li and 31P NMR, Phys. Rev. B 88 (5) (2013).
[13] V. Aravindan, J. Gnanaraj, Y.-S. Lee, S. Madhavi, $LiMnPO_4$ a next generation cathode material for lithium-ion batteries, J. Mater. Chem. A 1 (11) (2013) 3518.
[14] G. Cheng, J.D. Wilcox, T.J. Richardson, Improving the performance of lithium manganese phosphate through divalent cation substitution, Electrochem. Solid-State Lett. 11 (11) (2008) A190.
[15] M. Minakshi, S. Kandhasamy, Utilizing active multiple dopants (Co and Ni) in olivine $LiMnPO_4$, Curr. Opin. Solid State Mater. Sci. 16 (4) (2012) 163.
[16] T. Muraliganth, A. Manthiram, Understanding the shifts in the redox potentials of olivine $LiM_{1-y}M_yPO_4$ (M = Fe, Mn, Co, and Mg) solid solution cathodes, J. Phys. Chem. C 114 (36) (2010) 15530.
[17] I. Bilecka, M. Niederberger, Microwave chemistry for inorganic nanomaterials synthesis, Nanoscale 2 (8) (2010) 1358.
[18] K. Byrappa, T. Adschiri, Hydrothermal technology for nanotechnology, Prog. Cryst. Growth Charact. Mater. 53 (2) (2007) 117.
[19] C. Neef, C. Jaehne, H.-P. Meyer, R. Klingeler, Morphology and agglomeration control of $LiMnPO_4$ micro- and nanocrystals, Langmuir 29 (25) (2013) 8054.
[20] J. Chen, S. Wang, M.S. Whittingham, Hydrothermal synthesis of cathode materials, J. Power Sources 174 (2) (2007) 442.
[21] J. Chen, M.J. Vacchio, S. Wang, N. Chernova, P.Y. Zavalij, M.S. Whittingham, The hydrothermal synthesis and characterization of olivines and related compounds for electrochemical applications, Solid State Ionics 178 (31–32) (2008) 1676.
[22] A.V. Murugan, T. Muraliganth, P.J. Ferreira, A. Manthiram, Dimensionally modulated, single-crystalline $LiMPO_4$ (M = Mn, Fe, Co and Ni) with nano-thumblike shapes for high-power energy storage, Inorg. Chem. 48 (3) (2009) 946.
[23] C. Jaehne, C. Neef, C. Koo, H.-P. Meyer, R. Klingeler, A new $LiCoPO_4$ polymorph via low temperature synthesis, J. Mater. Chem. A 1 (8) (2013) 2856.

[24] C. Jaehne, R. Klingeler, Microwave-assisted hydrothermal synthesis of low-temperature $LiCoO_2$, Solid State Sci. 14 (7) (2012) 941.
[25] J. Rodriguez-Carvajal, An Introduction to the Program Fullprof 2000, The FullProf Team, 2001.
[26] J.M. Osorio-Guillen, B. Holm, R. Ahuja, B. Johansson, A theoretical study of olivine $LiMPO_4$ cathodes, Solid State Ionics 167 (3-4) (2004) 221.
[27] J.-H. Lee, H.-H. Kim, G.-S. Kim, D.-S. Zang, Y.-M. Choi, H. Kim, D.K. Yi, W.M. Sigmund, U. Paik, Evaluation of surface acid and base properties of $LiFePO_4$ in aqueos medium with pH and its elcetrochemical properties, J. Phys. Chem. C 114 (10) (2010) 4466.
[28] D.R. Lide, CRC Handbook of Chemistry and Physics, 84th ed., CRC Press, 2003.
[29] N. Wizent, G. Behr, F. Lipps, I. Hellmann, R. Klingeler, V. Kataev, W. Loeser, N. Sato, B. Buechner, Single-crystal growth of $LiMnPO_4$ by the floating-zone method, J. Cryst. Growth 311 (5) (2009) 1273.
[30] K. Wang, A. Maljuk, C.G. Blum, T. Kolb, C. Jaehne, C. Neef, H.-J. Grafe, L. Giebeler, H. Wadepohl, H.-P. Meyer, S. Wurmehl, R. Klingeler, Growth, characterization, and magnetic properties of a $Li(Mn,Ni)PO_4$ single crystal, J. Cryst. Growth 386 (2014) 16.
[31] R.D. Shannon, Revised effective ionic radii and systematic studies of interatomic distances in halides and chalcogenides, Acta Crystallogr. A 32 (1976) 751.
[32] R. Toft-Petersen, N.H. Andersen, H. Li, J. Li, W. Tian, S.L. Bud'ko, T.B.S. Jensen, C. Niedermayer, M. Laver, O. Zaharko, J.W. Lynn, D. Vaknin, Magnetic phase diagram of magnetoelectric $LiMnPO_4$, Phys. Rev. B 85 (22) (2012) 224415.
[33] D. Vaknin, J. Zarestky, J. Ostenson, B. Chakoumakos, A. Goni, P. Pagliuso, T. Rojo, G. Barberis, Weakly ($x = 0$) and randomly ($x = 0.033$) coupled using antiferromagnetic planes in $Li_{1-3x}Fe_xNiPO_4$ compounds, Phys. Rev. B 60 (2) (1999) 1100.
[34] J.H. Ranicar, P.R. Elliston, Spin-flopping in $LiMnPO_4$ and Cr_2BeO_4, Phys. Lett. 25 (10) (1967) 720.
[35] K. Su, F. Liu, J. Chen, Preparation of high performance carbon-coated $LiMnPO_4$ nanocomposite by an acetate-assisted antisolvent precipitation method, J. Power Sources 232 (2013) 234.
[36] J. Vetter, P. Novak, M.R. Wagner, C. Veit, K.C. Moeller, J.O. Besenhard, M. Winter, M. Wohlfahrt-Mehrens, C. Vogler, A. Hammouche, Ageing mechanisms in lithium-ion batteries, J. Power Sources 147 (1–2) (2005) 269.
[37] T. Kawamura, S. Okada, J. Yamaki, Decomposition reaction of $LiPF_6$-based electrolytes for lithium-ion cells, J. Power Sources 156 (2) (2006) 547.
[38] M.B. Pinson, M.Z. Bazant, Theory of SEI formation in rechargeable batteries: capacity fade, accelerated aging and lifetime prediction, J. Electrochem. Soc. 160 (2) (2012) A243.